Joule

CellPress

Article

Proton sponge promotion of electrochemical CO_2 reduction to multi-carbon products

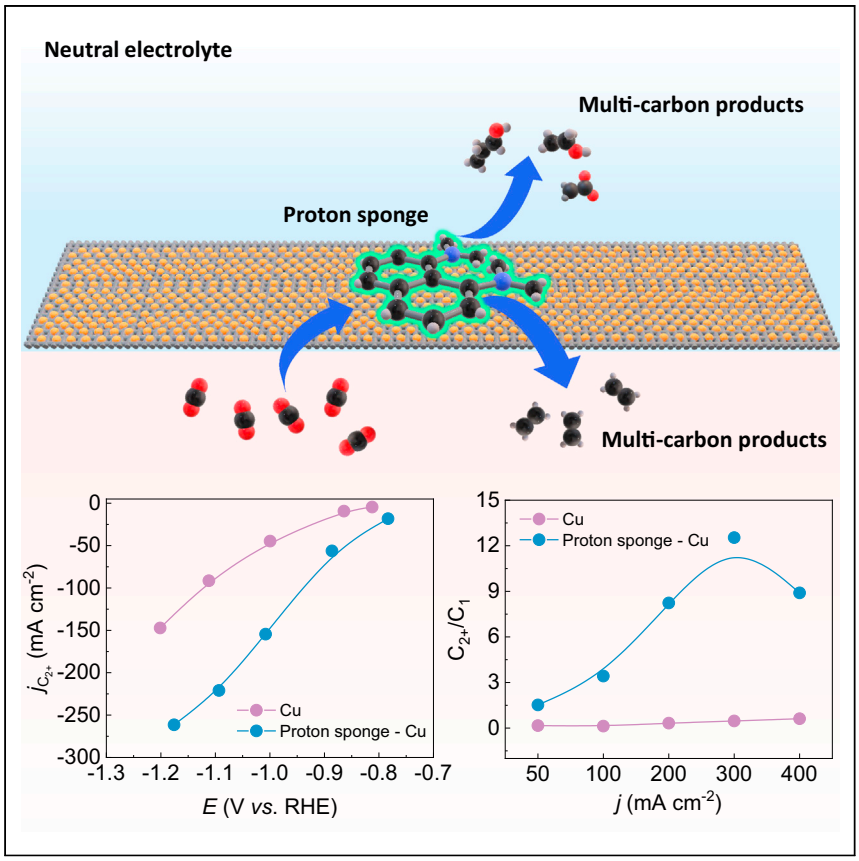

Using high-concentration alkaline electrolytes is a straightforward way to increase multi-carbon selectivity in electrochemical CO_2 reduction but is limited by the spontaneous reaction between CO_2 and hydroxide. Here, we developed an organosuperbase promotion strategy to increase the multi-carbon products selectivity in neutral electrolyte. The protonated organosuperbase stabilized *CO intermediates on the copper surface through a locally enhanced electrostatic field while maintaining a neutral pH bulk electrolyte to avoid extensive carbonate formation.

Lei Fan, Chun-Yen Liu, Peng Zhu, ..., Yingying Lu, Thomas P. Senftle, Haotian Wang

yingyinglu@zju.edu.cn (Y.L.)
tsenftle@rice.edu (T.P.S.)
htwang@rice.edu (H.W.)

Highlights

Organosuperbase-modified Cu promotes CO_2 electrocatalysis to multi-carbon products

Organosuperbase modification suppresses carbonate formation challenge

Protonated organosuperbases stabilize CO intermediates on Cu surface

Proton sponge modification presented a 20-fold improvement in C_{2+} to C_1 ratio

Fan et al., Joule 6, 1–16
January 19, 2022
https://doi.org/10.1016/j.joule.2021.12.002

Please cite this article in press as: Fan et al., Proton sponge promotion of electrochemical CO_2 reduction to multi-carbon products, Joule (2021), https://doi.org/10.1016/j.joule.2021.12.002

Joule

CellPress

Article

Proton sponge promotion of electrochemical CO_2 reduction to multi-carbon products

Lei Fan,[1,2,6] Chun-Yen Liu,[2,6] Peng Zhu,[2] Chuan Xia,[2,3] Xiao Zhang,[2] Zhen-Yu Wu,[2] Yingying Lu,[1,*] Thomas P. Senftle,[2,*] and Haotian Wang[2,4,5,7,*]

SUMMARY

High alkaline electrolytes have shown the potential to promote high-value C_{2+} products in the electrochemical CO_2 reduction reaction (CO_2RR), but the practical application is challenged by their strong CO_2 absorption with the electrolyte to form carbonate. By modifying the Cu catalyst surface with water-insoluble organosuperbases, such as thebis(dimethylamino)naphthalene "proton sponge," here, we change the interfacial microenvironment to stabilize adsorbed CO through a locally enhanced electrostatic field while maintaining a neutral pH electrolyte. Molecular dynamics (MD) with a reactive force field and density functional theory (DFT) calculations show that the CO intermediate is stabilized on the Cu surface by protonated organosuperbases, which promotes C_{2+} product formation over CO desorption. The organosuperbase-modified commercial Cu nanoparticle presented a 20-fold improvement in C_{2+} to C_1 ratio compared with its pristine performance, delivering a maximal C_{2+} faradic efficiency of ~80% and large partial current of over 270 mA cm^{-2} in neutral electrolyte.

Context & scale

Converting CO_2 into valuable fuels and chemicals with the energy input of renewable electricity is becoming a promising alternative route for sustainable production of chemicals and fuels. However, this electrocatalytic CO_2 reduction process is often challenged by low selectivity toward high-value multi-carbon products. This study proposes an effective and scalable "interfacial engineering" approach by simply mixing the catalyst with superbase molecules to improve the catalyst/electrolyte interfacial environmental for a favorable generation of multi-carbon products.

INTRODUCTION

Electrochemical reduction of CO_2 to value-added fuels and chemical feedstocks, powered by renewable energy, offers a potential solution to global climate change and the energy crisis.[1–5] State-of-the-art electrocatalysts with rationally designed electronic properties have been able to transform CO_2 into chemicals with high selectivity and activity, but most of the electrocatalysts can only drive two-electron reductions to C_1 products (i.e., carbon monoxide and formate).[6–9] Among different transition metals, copper-based materials attract the most attention due to their capability to reduce CO_2 molecules beyond C_1 products to high-value and high-energy-density C_{2+} hydrocarbons and oxygenates.[10–15] Promoting the C–C coupling step, which holds the key to generating C_{2+} products, is still an open challenge for improved C_{2+} product selectivity.[16–19]

To facilitate the C–C coupling step on copper surfaces, different catalytic materials engineering approaches, including morphology tuning,[20] crystal facet regulation,[21] oxidation state manipulation,[22] and heteroatom doping,[23] have been demonstrated to be effective. Beyond materials engineering, recent studies also found that, under a strong alkaline environment, electrochemical CO_2 reduction reaction (CO_2RR) selectivity to C_{2+} and activity can be dramatically improved,[24–28] which may be due to the formation of an abrupt interface or the high concentration of cations to induce local electrical field. While a strong alkaline electrolyte can promote

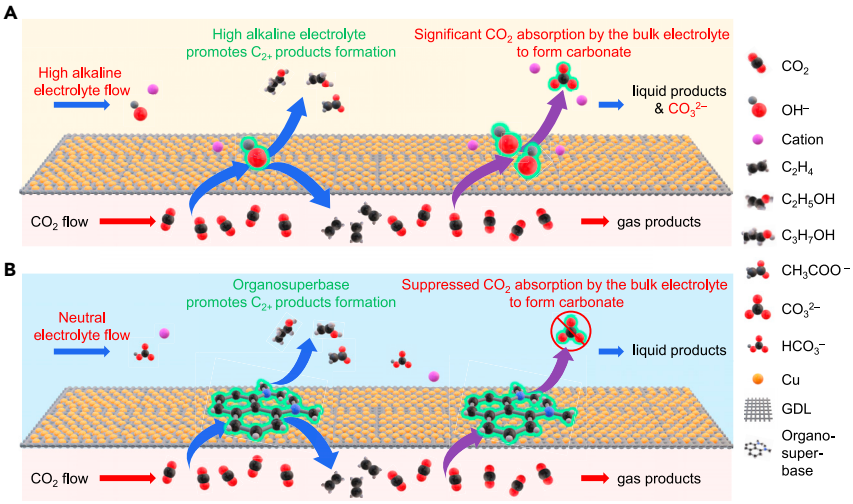

Figure 1. Schematic comparison of C–C coupling promotion effects through high alkaline electrolyte and organosuperbases

(A) High alkaline electrolyte can improve the CO_2RR to C_{2+} selectivity and activity. However, the strong alkaline electrolyte also causes significant CO_2 absorption due to the spontaneous reaction between OH^- and CO_2 at the electrolyte/CO_2 interface.

(B) Organosuperbase promotion of CO_2RR to C_{2+} products avoids the strong CO_2 absorption in the case of using high-pH bulk electrolyte.

industrially relevant generation rates of C_{2+} products, it also absorbs a significant amount of CO_2 gas during electrolysis due to the spontaneous reaction between OH^- and CO_2 at the electrolyte/CO_2 interface paying a large penalty of carbon and electrolyte losses (Figure 1A).[29–34]

Here, we report a facile interfacial engineering strategy to avoid the dilemma mentioned above between C–C coupling promotion and strong CO_2 absorption (Figure 1B). Instead of using the traditional inorganic base (such as potassium hydroxide [KOH]), we coat the Cu catalyst surface with water-insoluble organosuperbase molecules to change the microenvironment at the interface between electrolyte and catalysts for improved C_{2+} product selectivity while maintaining a neutral pH in the bulk electrolyte to avoid CO_2 absorption by alkaline solutions. The high alkaline superbase molecules can capture protons at the Cu/electrolyte interface in CO_2RR through neutralization reaction and thus form protonated organosuperbases.[35] These protonated organosuperbase molecules serve as positively charged modulators in CO_2RR, which can stabilize the key intermediates of C–C coupling process with locally enhanced electrostatic fields. As a result, copper catalysts modified with organosuperbases, such as 1,8-bis(dimethylamino) naphthalene (DMAN, also known as the "proton sponge"), presented a 20-fold improvement in C_{2+} to C_1 ratio compared with the pristine copper in neutral electrolyte, with a maximal C_{2+} faradic efficiency of ~80%, and a large C_{2+} partial current of over 270 mA cm^{-2}. Computational simulations, including both molecular dynamics (MD) with a reactive force field (ReaxFF)[36,37] and density functional theory (DFT), reveal details of how the superbase molecules modify the apparent electric field surrounding the adsorbed *CO molecule. The simulation results show that protonated organosuperbases are located close to the negative electrode surface in the reaction environment, which in turn induces a local electrostatic field that stabilizes *CO on the copper surface. This promotes the C–C coupling reaction step required for producing C_{2+} products.

[1]State Key Laboratory of Chemical Engineering, Institute of Pharmaceutical Engineering, College of Chemical and Biological Engineering, Zhejiang University, Hangzhou 310027, China

[2]Department of Chemical and Biomolecular Engineering, Rice University, Houston, TX 77005, USA

[3]Smalley-Curl Institute, Rice University, Houston, TX 77005, USA

[4]Department of Materials Science and NanoEngineering, Rice University, Houston, TX 77005, USA

[5]Department of Chemistry, Rice University, Houston, TX 77005, USA

[6]These authors contributed equally

[7]Lead contact

*Correspondence: yingyinglu@zju.edu.cn (Y.L.), tsenftle@rice.edu (T.P.S.), htwang@rice.edu (H.W.)

https://doi.org/10.1016/j.joule.2021.12.002

Please cite this article in press as: Fan et al., Proton sponge promotion of electrochemical CO_2 reduction to multi-carbon products, Joule (2021), https://doi.org/10.1016/j.joule.2021.12.002

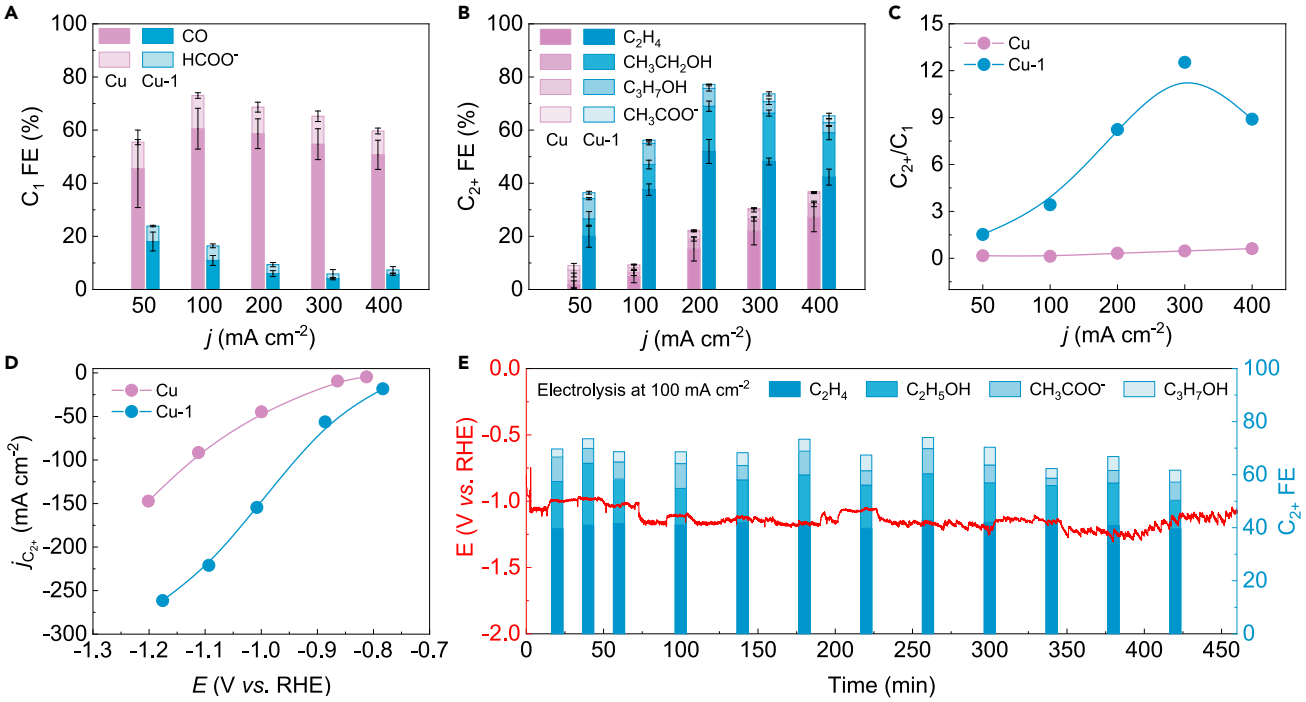

Figure 2. Electrochemical CO_2 reduction performance of Cu and DMAN-modified Cu (Cu-1)

(A and B) FEs of C_1 products and C_{2+} products on 25 nm Cu and Cu-1 at various current densities. The highest C_{2+} FE reaches 80% at 200 mA cm^{-2} on Cu-1.

(C) The C_{2+}/C_1 ratio of Cu and Cu-1. DMAN-modified Cu exhibits a 20-fold improvement compared with pristine Cu.

(D) Partial current densities of C_{2+} products on Cu and Cu-1. The highest C_{2+} partial current density is 270 mA cm^{-2} on Cu-1.

(E) Potential profile and C_{2+} FEs over 450-min continuous operation at 100 mA cm^{-2} on Cu-1. The error bars represent two independent tests.

RESULTS AND DISCUSSION

Impact of organosuperbase on C_{2+} selectivity on Cu

Apart from inorganic bases such as KOH, organosuperbases are another type of important base, which have been widely used as catalysts or bases in organic synthesis to improve the selectivity and activity of organic reactions.[35,38,39] DMAN, also known as the "proton sponge" because of its exceptional proton affinity, is one of the most attractive organosuperbase.[35] DMAN is water insoluble, commercially available, and already produced at a large scale with low price.[40] Therefore, we first employed DMAN as a model organosuperbase molecule to study the promotion effects for C–C coupling on Cu catalyst. Commercially available 25-nm copper nanoparticles (Cu-NPs) were used as the pristine CO_2RR catalyst. DMAN was dissolved in isopropanol and then mixed with Cu-NPs to ensure a uniform coating on the copper surface. This mixture catalyst was air-brushed onto a gas-diffusion-layer electrode with a mass loading of about 0.7 mg cm^{-2}. The electrocatalytic performance was studied in a standard three-electrode flow cell (Figure S1), and 1.0 M aqueous potassium bicarbonate ($KHCO_3$) was used as the neutral pH electrolyte (used for all tests). Gaseous and liquid products were detected by gas chromatography (GC) and nuclear magnetic resonance (NMR), respectively (see experimental procedures). The I-V curves of pristine Cu-NPs and DMAN-coated Cu-NPs (Cu-1) showed very similar CO_2RR activity, delivering a maximum current density of 400 mA cm^{-2} at −1.2 V versus reversible hydrogen electrode (versus RHE) (Figure S2). It was not surprising that the major CO_2RR product from pristine Cu-NPs was CO (FE ~60%) at all applied current densities, whereas the FEs of total C_1 products (CO and formate) were about 60% to 70%. With the overpotential gradually increased, the C_{2+} FE increased from 10% to 35%, which was still much lower than that of C_1 products (Figure 2A). This result agrees

Please cite this article in press as: Fan et al., Proton sponge promotion of electrochemical CO_2 reduction to multi-carbon products, Joule (2021), https://doi.org/10.1016/j.joule.2021.12.002

with previous reports and shows that the C–C coupling process is not preferred on the pristine copper surface at neutral electrolyte, even in flow cell.[15] After a direct mixture with DMAN, the modified Cu catalyst presented a dramatically improved C_{2+} product selectivity and suppressed C_1 selectivity across the entire electrochemical potential window, forming a sharp contrast with pristine Cu-NPs. As shown in Figures 2A and 2B, DMAN-modified Cu catalysts delivered a peak C_{2+} FE of ~80% and low C_1 selectivity of ~10% at 200 mA cm^{-2}, suggesting a 25-fold improvement in C_{2+}/C_1 ratio compared with that of pristine Cu (Figure 2C), which is much better than the pristine Cu in an alkaline electrolyte (1.0 M KOH, Figure S3). Specifically, we found that the FE of each C_{2+} product was improved after the addition of organosuperbase molecule (at 200 mA cm^{-2}): the C_2H_4 FE increased from 15% to 52%, ethanol from 4% to 17%, n-propanol from to 3% to 7%, and acetate from 0.5% to 1.5% (Figure S4). As a result, the single pass efficiency of Cu-1 toward C_{2+} products was much higher than that of pristine Cu (Figure S5). While the distribution of CO_2RR products was dramatically changed, the H_2 FEs were similar for these two catalysts (Figure S6), suggesting that the organosuperbase molecule might only impact the C–C coupling step on the Cu surface. Additionally, the onset potential of C_2H_4 was improved from −0.57 to −0.43 V (Figure S7), indicating the promoted C–C coupling kinetics by organosuperbase modification. Because of this high C–C coupling efficiency, the maximum C_{2+} partial current density of our DMAN-modified Cu reached 270 mA cm^{-2} in a neutral pH solution (Figure 2D). We also demonstrated the stability of DMAN-modified Cu-NPs. A 450-min CO_2RR electrolysis was continuously and stably operated under 100 mA cm^{-2} current, maintaining over 60% C_{2+} FEs with negligible degradation in overpotential (Figures 2E and S8).

Characterizations of catalysts

The morphology, crystallinity, and electronic structure of catalysts may impact their CO_2RR performances in different ways. To exclude these factors, we first used scanning electron microscopy (SEM) and transmission electron microscopy (TEM) to observe whether there are any morphological changes after the mixture with organosuperbase molecules. As shown in Figures S9 and S10, organosuperbase did not change the morphology of Cu-NPs before and after CO_2RR electrolysis. We also used X-ray diffraction (XRD) to study the crystal structure of Cu-NPs. The Cu-NPs were in the form of Cu/Cu_2O mixture for both Cu-NPs and Cu-1 before CO_2RR and were both *in situ* reduced to metallic Cu under CO_2RR conditions (Figure S11), as confirmed by X-ray photoelectron spectroscopy (XPS; Figure S12). These results indicate that the organosuperbase modification does not change the morphology, crystallinity, and oxidation states of the Cu-NPs. We also evaluated the stability of DMAN organosuperbase under CO_2RR conditions. After CO_2RR, the electrode was dried and immersed in d_6-DMSO (deuterated dimethyl sulfoxide) solutions for NMR analysis. As shown in Figure S13, the chemical structure of DMAN does not change after electrolysis, suggesting a high stability under CO_2RR conditions. From those characterization results, we were convinced that the properties of the Cu-NP materials were not changed after the addition of superbase molecules, and no chemical reactions were observed between Cu and superbase molecules. These results indirectly suggest that the improved C–C coupling step could be related to the molecular effects that our superbase molecule introduced.

Characterizations of organosuperbase promotion effects

To further validate and better understand the organosuperbase promotion effects, a series of control experiments have been performed. We first excluded other possible side reactions by using DMAN-coated gas-diffusion electrode (GDE) as a control sample electrode. In Figures S14 and S15, GC and NMR results show that DMAN

Please cite this article in press as: Fan et al., Proton sponge promotion of electrochemical CO_2 reduction to multi-carbon products, Joule (2021), https://doi.org/10.1016/j.joule.2021.12.002

itself exhibits no activity for CO_2RR. We also tested CO_2RR performance on Cu-1 catalyst using argon as a feedstock, and, as a result, there were no gas-phase or liquid-phase products, suggesting that no side reactions occurred under electrochemical reduction conditions. Besides, we also changed the electrode preparation process to further explore the organosuperbase impacts. Instead of mixing them together, we first air-brushed Cu nanoparticles and then catalyst surface was coated with the organosuperbase molecules. As shown in Figure S16, the C_{2+} FEs of this electrode were also much improved compared to the pristine Cu-NP electrode. However, the promotion effect was not as good as the mixing method because only the top layer of Cu-NPs can be covered by the organosuperbase. We also varied the loading of DMAN on the Cu surface. We found that C_{2+} FE gradually increased against the surface coverage ratio of the DMAN on Cu and reached the maximum values when the mass ratio was ~0.5 (Figure S17). In contrast, CO FE gradually decreased against the increased mass ratio of DMAN and Cu-NPs. A further increase of DMAN coverage led to a drop of C_{2+} selectivity (i.e., organosuperbase/Cu mass ratio = 1), which might be due to the limited Cu sites for CO dimerization. Electrochemical double-layer capacitance measurements showed that the electrochemically active surface areas of Cu and Cu-1 are similar, which indicated that the active sites of Cu would not be influenced at the optimized organosuperbase/Cu ratio (Figure S18). Besides, the possible impact of cations as the electrolytes in the solution has also been excluded because the same electrolytes were employed for all samples. Taken together, we can confirm that the increased C_{2+} selectivity originates from the surface interaction between organosuperbase molecule and Cu.

To explore whether the effect of this DMAN superbase molecule on electrochemical reduction of CO_2 to C_{2+} products is a general effect or not, we modified the Cu-NPs with two other organosuperbase molecules with different chemical structures, including guanidine-type organosuperbase (TBD: 1,5,7-triazabicyclo[4.4.0]dec-5-ene), hybrid organosuperbase (TMGN: 1,8-bis(tetramethylguanidino)naphthalene; hybrid means this molecular combines the proton sponge skeleton with the guanidine group), and one non-organosuperbase molecule with similar chemical structure (DMNA: N,N-dimethyl-1-naphthylamine) (Figure 3A). After the coating with other organosuperbases, i.e., TBD and TMGN, the selectivity of C_1 products also decreased and C_{2+} FE increased (Figures 3B, 3C, S19, and S20), suggesting a similar effect to the DMAN superbase molecule. For non-organosuperbase-modified Cu-NP (Cu-4), i.e., DMNA, which is only one amine ligand different from DMAN, its CO_2RR to C_{2+} product selectivity showed no improvements compared with pristine Cu (Figures 3B, 3C, and S21). The FEs of H_2 were similar for all samples (Figure S22). This result clearly suggests that the basicity of these water-insoluble molecules plays a key role in improving C–C coupling step on Cu surface, which is further illustrated by the following computational simulations.

We further tested whether this "proton sponge" modification strategy could be extended to other Cu catalysts such as Cu-NPs with larger sizes (60–80 nm) and polycrystalline Cu nanocubes with (100) facet exposed (Cu-NCs).[41] The promotion effects on larger-sized Cu-NP (Figure S23A) are quite similar to the smaller one we tested, as shown in Figures S23B–S23D, as they were both exposed with (111) facets. The starting point of pristine Cu-NCs (Figure S24A) was already much improved compared with Cu-NPs under all current densities with a peak C_{2+} product FE of 65% at 300 mA cm^{-2} (Figures S24B–S24D). This result agrees well with our previous report that the Cu(100) facet is more selective for C–C coupling than the Cu(111) facet.[21] By coupling the superbase molecule promotion effects with the facet effects, the C_{2+} FE was further improved to ~80% within a wide range of current

Please cite this article in press as: Fan et al., Proton sponge promotion of electrochemical CO_2 reduction to multi-carbon products, Joule (2021), https://doi.org/10.1016/j.joule.2021.12.002

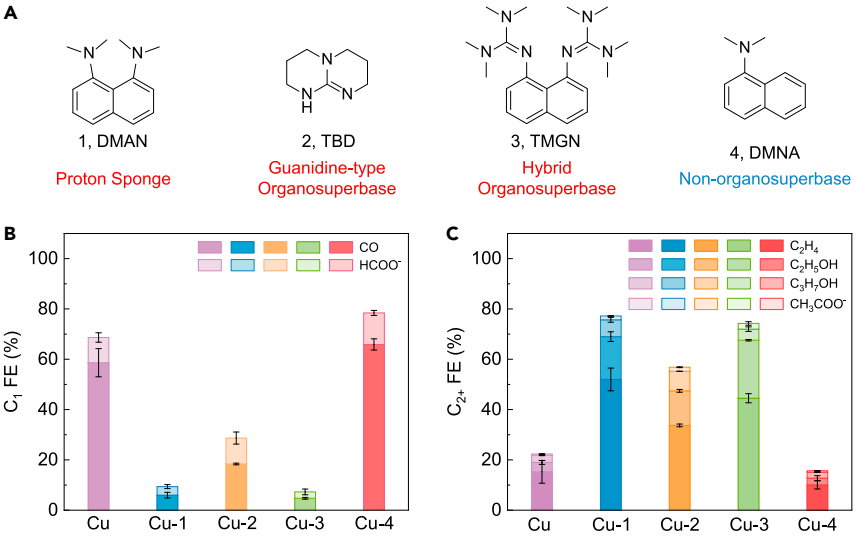

Figure 3. CO_2RR performance on different organosuperbase-modified Cu

(A) Chemical structures of different types organosuperbases and non-organosuperbase.

(B and C) FEs of CO_2RR products on different catalysts at 200 mA cm^{-2}. Compared with pristine Cu nanoparticles, three different types of organosuperbase-modified Cu presents enhanced C_{2+} selectivity, whereas non-organosuperbase exhibited no promotion effects toward C_{2+} products. The error bars represent two independent tests.

densities from 100 to 300 mA cm^{-2} (Figure S25). The maximum C_{2+}/C_1 ratio was 18 at 400 mA cm^{-2}, and C_{2+} partial current density can reach 287 mA cm^{-2} (Table S1).

Theoretical investigation of organosuperbase promotion mechanism

We first investigated whether each of the organosuperbases would be protonated or deprotonated at the electrode surface under an applied potential by determining thermodynamics and kinetics associated with deprotonating the superbase. This was done by computing the pK_a value of each base to determine whether it would exist in the protonated state at the bulk pH. We then computed the kinetic deprotonation barrier to determine whether the bases could be deprotonated by a reduction of the proton at the negative electrode surface (i.e., $BH^+ + e^- + * \rightarrow B + *H$, where B represents the base and * represents a surface site). The pK_a of each organosuperbase was computed with atom-centered DFT at the B3LYP/6–311++G level of theory[42,43] with solute charge density (SMD) solvation.[44] Kinetic barriers for organosuperbase deprotonation at the surface were computed using plane-wave basis sets and the GGA-PBE exchange-correlation functional.[45] Full computational details are reported in the experimental procedures section. In the search for the transition state for organosuperbase deprotonation, we found that the proton is most favorably transferred to the surface through an explicit water molecule shuttle that forms a hydronium-like transition state (Figure S26). The electrochemical deprotonation barrier was found to correlate with the computed pK_a values, as expected (Figure S27). Here, among all tested molecules, we observe that DMNA has the lowest pK_a, and deprotonation is barrierless at –1.0 V versus RHE, which implies that DMNA readily loses its proton via reduction at the Cu(111) surface. We note that the local pH at the copper electrodes may be different from the pH in bulk solution, and our estimation of deprotonation barrier can change accordingly. However, the barriers are shifted simultaneously; therefore, the difference between each organosuperbase remains unchanged. Thus, we conclude that DMNA at the surface is mostly deprotonated given the lowest deprotonation barrier, and the other three bases

remain protonated, which is consistent with the observation that DMNA is ineffective for enhancing selectivity to C_{2+} products.

The trajectory of the protonated and deprotonated superbases in the aqueous phase above the surface was investigated by MD simulations with the ReaxFF force field[36,37] (Figures 4A and 4B). The charge of the atoms in the simulation cell were determined through the charge equilibration scheme used in the functional form of ReaxFF. Charge distributions were constrained to represent the reaction conditions in the following manner. The Cu slab was constrained to have an overall negative charge, which was varied in separate simulation trials to assess the effect of negative surface charge density on the trajectory of the superbase above the surface (Figures 4C and S28). The protonated organosuperbase was constrained to have a positive charge, and the water molecules each were neutral. In each simulation, the charges of individual atoms were initially determined with a full charge equilibration and were then fixed during the MD simulations for computational efficiency (see the experimental procedures section for more details). Figure 4C shows that DMAN migrates around the solution when no external electric field is applied but remains near the double-layer surface once an applied potential (i.e., negative surface charge density) exists. Similar behavior was observed for all four bases, which was verified in each case by three independent MD simulations starting with different water configurations (Figure S28). Deprotonated organosuperbases are neutral; thus, their trajectories do not depend on the applied potential (Figure S29). Therefore, the protonated organosuperbases attach more readily to the surface under electrochemical conditions. Because DMNA is reduced and deprotonated at the surface, we do not expect it to remain attached to the surface to the same degree as the other three bases. This is consistent with the absence of C_{2+} promotion in the case of DMNA, despite its structural similarities to the other bases.

Next, we investigated the local electric field induced by the base molecules that remain near the double-layer, as this effect is known to enhance C–C coupling.[46,47] We found that the protonated organosuperbases create a planar-averaged local electric field of about -1 V Å^{-1} at the height of the center of the adsorbed CO molecule (Figure 4D). The distribution of the induced electric field at the position of the CO* intermediate is plotted in Figure 4E to show the magnitude of electric field at each location above the surface. Using the optimized structure of the protonated organosuperbase, water molecules, and Cu slab, we further investigated the contribution of each component on the local electric field by single-point calculations with each individual component successively removed. When only water molecules are present above the Cu slab, the planar-average electric field is -0.49 V Å^{-1} at the height of the *CO molecule (dash-dot lines in Figure 4D). When the deprotonated organosuperbase is added, the electric field is enhanced to -0.69 V Å^{-1} (dashed lines in Figure 4D). However, the deprotonated molecules are neutral and thus are not strongly drawn to the negative copper surface, as shown by the MD simulations in Figure S29. Thus, only the organosuperbases that remain protonated under electrochemical reaction conditions, i.e., DMAN, TBD, and TMGN, enhance the local electric field close to the copper surface.

Aqueous cations have been reported in the literature[46–48] to enhance CO_2 electrochemical reduction by creating electrostatic fields. Resasco et al.[47] demonstrated that the impact of electric field depends on the dipole moment of the adsorbed species, with *OCCO formation and *CO-binding strength being promoted as the electric field is enhanced. This agrees with our experimental result and DFT analysis (Figure S30). In the experimental results (Figure 3), CO production was suppressed when

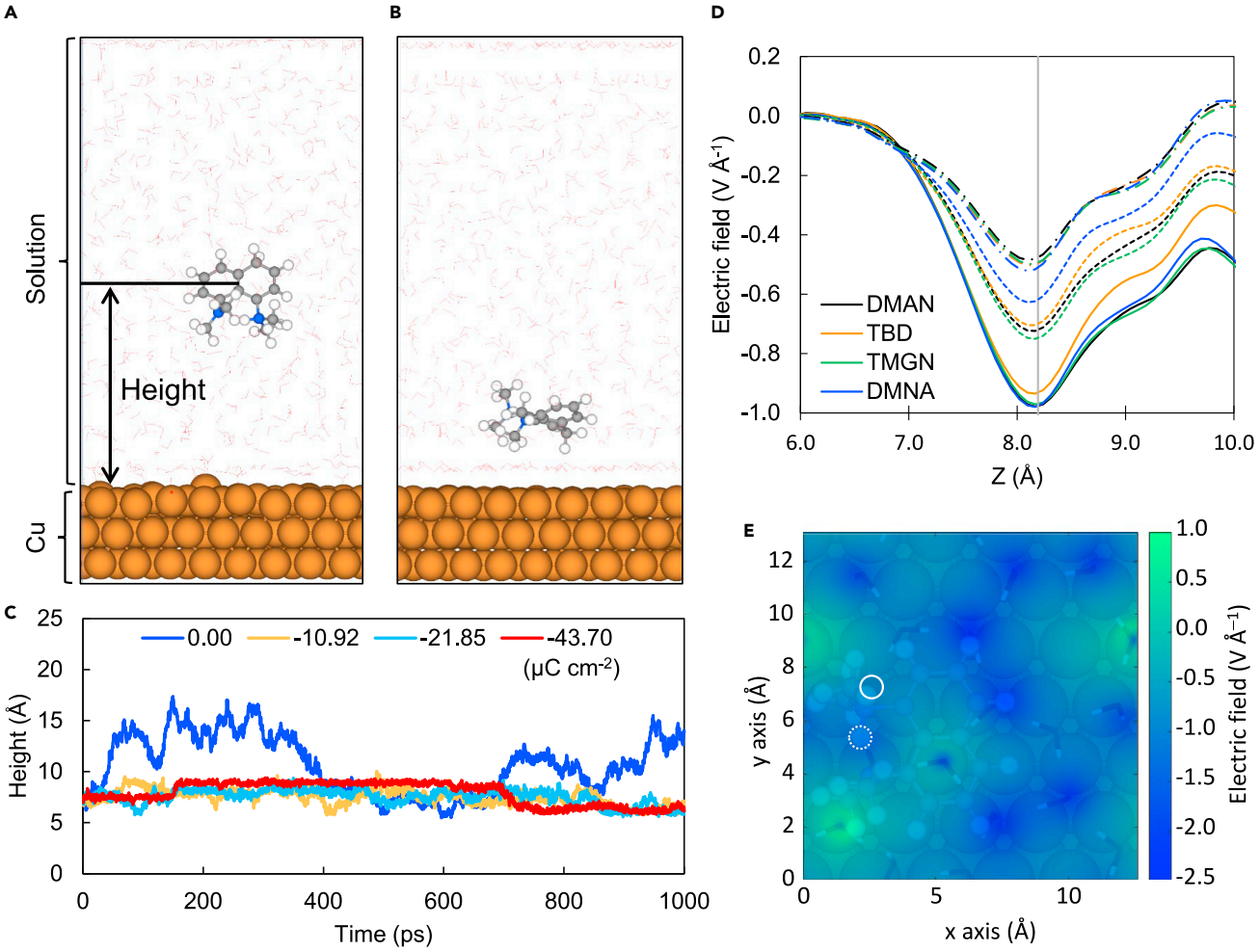

Figure 4. Demonstration of the trajectory of superbase molecules with molecular dynamic simulations and their impact on local electric field

(A and B) Positions of protonated DMAN in the aqueous phase above the Cu surface at (A) 0.00 μC cm^{-2} and (B) −43.70 μC cm^{-2} after 1 ns. Water molecules are shown with line models to improve the visibility of the base molecules.

(C) The distance between protonated DMAN and Cu substrate on the z axis under various assigned surface charges. The topmost surface Cu atoms are located at 0 Å.

(D) Planar-averaged electric field in the presence of the protonated (solid line) and deprotonated (dashed line) organosuperbases, as compared with that computed in the presence of just the solvating water molecule (dash-dot line). The center of CO molecule is indicated by a vertical line in gray.

(E) 2D map of the electric field in the presence of protonated DMAN computed at the height of the center of the CO molecule. The projected position of CO and proton in organosuperbase is marked by the white solid and dashed circle, respectively.

the organosuperbases, i.e., DMAN, TBD, and TMGN, were introduced. We hypothesize that *CO is stabilized by the electrostatic field induced by the organosuperbases. The *CO further undergoes C–C coupling reaction, i.e., *CO + *CO → *OCCO, which is more favorable under the induced electric field.[47] The CO-binding energy with the presence of organosuperbases is plotted against the estimated electric field, e.g., extracting the value in white solid circle in Figure 4E, in Figure S30. The data points fit the curve derived from the energy obtained from the vacuum copper surface with an explicit applied external potential (to within 0.1 eV accuracy). This further suggests that the electrostatic field causes the *CO-binding strength enhancement.

From the theoretical investigation, we conclude that DMNA resides in a deprotonated form and thus does not remain on the copper surface; thus, it has no effect

Please cite this article in press as: Fan et al., Proton sponge promotion of electrochemical CO_2 reduction to multi-carbon products, Joule (2021), https://doi.org/10.1016/j.joule.2021.12.002

on the selectivity toward multi-carbon products. Nevertheless, the lower selectivity enhancement of TBD compared with DMAN and TMGN cannot be explained by the MD simulations and electrostatic field enhancement. For this reason, we also studied the solubility of the organosuperbases by extracting the single-point solvation energy for each organosuperbase in both protonated and deprotonated form (Figure S31). The results show that TBD is the least hydrophobic of the organosuperbases and therefore tends to reside in the solution phase more than the other bases do. Therefore, its effect diminishes compared with DMAN and TMGN, whose hydrophobic nature further drive them toward the surface. DMAN and TMGN are strongly hydrophobic and remain protonated near the surface; thus, they most significantly enhance the selectivity toward multi-carbon chemicals.

Conclusion

In summary, this work demonstrates a simple, inexpensive, and scalable strategy to significantly improve the C_{2+} product selectivity in CO_2RR without the use of strong alkaline electrolyte. The use of "proton sponge," as well as other organosuperbases, showed significantly improved CO_2RR to C_{2+} products conversion while avoiding the strong CO_2 absorption challenge in strong alkaline electrolytes. Theoretical results showed that a *CO intermediate for an ongoing C–C coupling process is well stabilized by organosuperbases. Given the simple catalyst preparation process, the organosuperbase modification method is promising for scalable electrocatalyst synthesis. Considering the exceptional basicity of organosuperbase, we believe that this strategy could be further extended to other electrochemical reactions, especially for those where alkaline electrolytes promote the reaction but induce undesirable side reactions.

EXPERIMENTAL PROCEDURES

Resource availability

Lead contact

Further information and requests for resources and materials should be directed to and will be fulfilled by the lead contact, Haotian Wang (htwang@rice.edu).

Materials availability

The materials generated in this study can be made available upon reasonable request.

Data and code availability

The geometries for deprotonation barrier estimation and the electric field computation, as well as the initial configutation of MD simulations, are collected at https://github.com/tsenftle/CO_Superbase. The data that support the findings of this study are available from the corresponding authors upon reasonable request.

Electrode and catalyst preparation

20-mg organosuperbase (Sigma-Aldrich) was first dissolved in 5-mL isopropanol, then 40-mg Cu-NPs or Cu_2O nanocubes and 160-μL binder solution (nafion 117 [Sigma-Aldrich, 5%]) was added, and the solution was sonicated for 20 min to obtain a homogeneous ink. Then, ~0.7 mg cm^{-2} catalyst was loaded on Sigracet 39 BB gas-diffusion-layer (GDL) electrode (Fuel Cell Store). 25 and 60–80 nm Cu-NPs were purchased from Sigma-Aldrich. Cu nanocube was synthesized using the following method: deionized water (100 mL), $Cu(NO_3)_2$ solution (0.1 M, 5 mL), sodium dodecyl sulfate (0.87 g), hydroxylammonium chloride solution (0.2 M, 3 mL), and sodium hydroxide solution (1 M, 1.8 mL) were added to a reactor in the order list, and the mixture was held for 2 h at room temperature. Cu_2O nanocube was obtained by

Please cite this article in press as: Fan et al., Proton sponge promotion of electrochemical CO_2 reduction to multi-carbon products, Joule (2021), https://doi.org/10.1016/j.joule.2021.12.002

centrifugation and washed using isopropanol and water for three times. The final product was dried in vacuum. Before CO_2RR test, the Cu_2O nanocubes were *in situ* reduced to metallic Cu-NC at 200 mA cm^{-2} in the flow cell.

Characterization

Powder XRD data were collected using a Bruker D2 PHASER diffractometer in parallel beam geometry employing Cu Kα radiation (wavelength 1.54056 Å) and a one-dimensional LYNXEYE detector, at a scan speed of 0.02° per step and a holding time of 1 s per step, XPS was obtained with a PHI Quantera spectrometer, using a monochromatic Al Kα radiation (1,486.6 eV) and a low-energy flood gun as neutralizer. All XPS spectra were calibrated by shifting the detected carbon C 1 s peak to 284.6 eV. SEM was performed on a FEI Quanta 400 field emission scanning electron microscope. TEM was performed on a JEOL 2100 transmission electron microscope under 200 kV. NMR spectral of the organosuperbase tested on Bruck 500MHz spectrometer using d_6-DMSO (Sigma-Aldrich) as the solvent.

Electrochemical measurements

All electrochemical measurements were run at 25°C in a customized flow cell separated by nafion 117 membrane (Fuel Cell Store). A BioLogic VMP3 workstation was employed to record the electrochemical response. Certain amounts of $KHCO_3$ (Sigma-Aldrich, 99.95%) were dissolved in Milli-Q water to prepare the 1.0 M electrolyte. In a typical three-electrode test system, a nickel foam and a saturated calomel electrode (SCE) were used as the counter and reference electrode, respectively. For long-term stability test, IrO_2-coated GDL (Fuel Cell Store) was used as the anode. All potentials measured against SCE were converted to the RHE scale in this work using E(versus RHE) = E(versus SCE) + 0.244 V + 0.0591 × pH, where pH values of electrolytes were determined by an Orion 320 PerpHecT LogR Meter (Thermo Scientific). Solution resistance (R_u) was determined by potentiostatic electrochemical impedance spectroscopy (PEIS) at frequencies ranging from 0.1 Hz to 200 kHz and manually compensated as E (iR corrected versus RHE, where iR is the voltage drop from electrolyte resistance, 90% iR correction was used for all correction) = E (versus RHE) − R_u × I (current). The double-layer capacitances for different catalysts were tested in Ar-saturated 1 M $KHCO_3$ after pre-reduction at 50 mA cm^{-2} for 20 min.

CO_2 reduction product analysis

To quantify the gas products during electrolysis, CO_2 gas (Airgas, 99.995%) was delivered into the cathodic compartment at a rate of 50.0 standard cubic centimeters per minute (sccm, monitored by Alicat scientific mass flow controller) and vented into a GC (GC, Shimadzu GC-2014) equipped with a combination of molecular sieve 5A, HayeSep Q, HayeSep T, and HayeSep N columns. A thermal conductivity detector (TCD) was mainly used to quantify H_2 concentration, and a flame ionization detector (FID) with a methanizer was used to quantitative analysis CO content and/or any other alkane species. The partial current density for a given products was calculated as below:

$$j_i = x_i \times v \times \frac{n_i F p_o}{RT} \times (electrode\ area)^{-1}$$

where x_i is the volume fraction of certain product determined by online GC referenced to calibration curves from the standard gas sample (Airgas), ϑ; is the flow rate of 50.0 sccm, n_i is the number of electrons involved, p_o = 101.3 kPa, F is the faradic constant, T = 298 K, and R is the gas constant. The corresponding faradic efficiency at each potential is calculated by FE = $\frac{j_i}{j_{total}}$ × 100%.

Please cite this article in press as: Fan et al., Proton sponge promotion of electrochemical CO_2 reduction to multi-carbon products, Joule (2021), https://doi.org/10.1016/j.joule.2021.12.002

1D 1H NMR spectra were collected on an Agilent DD2 600 MHz spectrometer to quantify the liquid products. Typically, 500 μL of electrolyte after electrolysis were mixed with 100 μL of D_2O (Sigma-Aldrich, 99.9 atom % D) and 0.03 μL DMSO (Sigma-Aldrich, 99.9%) as internal standard.

Molecular dynamic simulations

We applied MD with the ReaxFF potential[36,37] to investigate the trajectory of protonated and deprotonated organosuperbases under an applied potential. The force field describing the atomic interactions was developed by Wen et al..[49] The Berendsen thermostat was used with a time step of 0.25 fs for all MD simulations in an NVT ensemble. A copper slab with three layers, 500 water molecules, and one protonated/deprotonated organosuperbase molecule were placed in a 20.16 × 21.82 × 40 $Å^3$ unit cell, as illustrated in Figures 4A and 4B. The bottom layer of the copper slab was fixed. The number of water molecules was chosen to match the bulk density of water at 1 g cm^{-3}. We first conducted the NVT simulations with full charge equilibration executed at each time step, where constraints were applied to maintain a constant negative charges of the entire copper slab, a positive charge of +1 on the protonated organosuperbase, a charge of 0 on the deprotonated organosuperbase, and neutral water molecules. However, we found that the results were not affected if we fixed the charge of each atom with values determined from separate charge equilibration steps. Thus, we chose to fix the charges of each atom after the initial charge equilibration, which is computationally efficient. The charge of each copper atom was assigned to be 0 *e*, −0.025 *e*, −0.05 *e*, and −0.1 *e* (*e* is the positive elementary charge), representing different applied potentials. The correlation between surface charge density and applied potential, shown in Figure S32, is in agreement with the literature.[50] The charge of individual atoms in protonated/deprotonated organosuperbase and water molecules was determined by the charge equilibrium using ReaxFF potential when the constraints were applied and the molecule was in an isolated unit cell. For instance, the overall charge of water molecule is neutral, but the charges on H and O are +0.31 and −0.62, respectively. The MD simulations for each organosuperbase molecule in protonated and deprotonated form were conducted for 1 ns in three independent trials with different initial configuration of water molecules (Figures S28 and S29).

Density functional theory

The Vienna *ab initio* simulation package (VASP 5.4.4)[51] was used to estimate the deprotonation barrier of the organosuperbases and their impact on the local electric field. The core electrons were treated by the projector augmented-wave (PAW) method[52] and VASP default potential.[53] The explicitly treated valence electrons are as follows: C – $2s^2 2p^2$, Cu – $3d^{10} 4s^1$, H – $1s^1$, O – $2s^2 2p^4$, and N – $2s^2 2p^3$, which were described by generalized gradient approximation (GGA) with Perdew-Burke-Ernzerhof (PBE) exchange-correlation functional[45] and spin polarization. The plane-wave basis set was truncated at 400 eV kinetic energy cutoff. The Brillouin zone was sampled by 1 × 1 × 1 Monkhorst-Pack (MP)[54] k-points sampling for Cu(111) surfaces. A dipole correction was applied in the z direction to prevent slab-slab interactions. Grimme's D3 dispersion correction was used to treat van der Waals interactions.[55] Geometries of adsorbed superbases used to estimate the local electric field were optimized until the maximum force between the atoms was less than 0.02 eV $Å^{-1}$. The criterion for geometry optimization for transition state search was 0.05 eV $Å^{-1}$. The energy of CO and H_2 was computed in a 15 × 16 × 17 $Å^3$ unit cell with 1 × 1 × 1 MP k-points sampling.

Three-layer Cu(111) was used to represent the metal surface with the bottom layer fixed. The distance between the Cu slabs in z direction was set to be greater than 15 Å in all

Please cite this article in press as: Fan et al., Proton sponge promotion of electrochemical CO_2 reduction to multi-carbon products, Joule (2021), https://doi.org/10.1016/j.joule.2021.12.002

instances. From the MD simulations, we determined that one water layer would be present between the Cu(111) surface and the organosuperbases. Thus, for local electric field estimation, we first optimized a system with a protonated organosuperbase, adsorbed CO species, Cu(111) slab, and an explicit water layer between the metal surface and the organosuperbase. We note that the unit cell was overall neutral, the surface is negative, and the protonated organosuperbase is positively charged. The optimized geometry was used to compute the electric field and the CO-binding energies with single-point calculations. For the deprotonation barrier calculations, we used another surface model with two explicit water molecules acting as a hydrogen shuttle placed with a protonated organosuperbase above the Cu(111) surface.

The translational, rotational, and vibrational entropy corrections were included for gaseous CO and H_2 with standard formulas derived from the statistical mechanics. Only vibrational contributions were used for adsorbed species. Climbing image nudged elastic band (CI-NEB)[56] was used to search for transition state. To compute the electrochemical barriers, we applied the method developed by Janik and coworkers,[57–59] which is described in the next section.

We used Gaussian16 program package[60] to compute the pK_a of each organosuperbase. The geometries of pristine and protonated molecules were optimized at the B3LYP/6–311++G level of theory[42,43] with the SMD[44] implicit solvation model. Two additional water molecules were included to represent explicit solvation. The free energy of protonation (ΔG) and pK_a were computed at 298.15 K using the following equation:

$$\Delta G = G_{H^+ - organosuperbase} + G_{2H_2O} - G_{organosuperbase} - G_{H^+ - 2H_2O}$$

$$pKa = -\frac{\Delta G}{RT/\log_{10}(e)}$$

where $G_{H+\text{-}organosuperbase}$ is the free energy of the protonated superbase, G_{2H2O} is the free energy of two explicit water molecules, $G_{organosuperbase}$ is the free energy of pristine superbase, $G_{H+\text{-}2H2O}$ is the free energy of hydronium with an extra water molecule, R is the gas constant, and T is the temperature.

Electrochemical barrier for deprotonation of superbase molecules

Deprotonation barriers were computed by the method developed by Janik and coworkers.[57–59] We first used a geometry with two explicit water molecules and the organosuperbase above the Cu(111) surfaces to compute the reference equilibrium potential (U^0) for forming the protonated organosuperbase on the RHE scale:

$$U^0 = -\frac{G_{H^+ - organosuperbase - water - Cu(111)} - G_{organosuperbase - water - Cu(111)} - \frac{1}{2}G_{H_{2(g)}}}{e}$$

where $G_{H^+ - organosuperbase - water - Cu(111)}$ is the free energy of protonated organosuperbase with two explicit water molecules on the Cu(111) surface, $G_{organosuperbase - water - Cu(111)}$ is the free energy of deprotonated organosuperbase with two explicit water molecules on Cu(111) surface, and $G_{H_{2(g)}}$ is the free energy of gaseous H_2 at 298 K and 1 atm. Once the transition state is found by CI-NEB simulation,[56] the activation energy ($\Delta G^{act}(U)$) at the potential U versus RHE is calculated as:

$$\Delta G^{act}(U) = \Delta G^{act}\left(U^0\right) + \beta \times \left(U - U^0\right)$$

where β is the reaction symmetry factor (assumed to be 0.5 in this work). The computed values of U^0 and the deprotonation barriers are listed in Table S2, and

Please cite this article in press as: Fan et al., Proton sponge promotion of electrochemical CO_2 reduction to multi-carbon products, Joule (2021), https://doi.org/10.1016/j.joule.2021.12.002

the optimized geometries used to compute the deprotonation barriers are shown in Figure S26.

Surface charge density and applied potential

The relationship between the surface charge density and the applied potential is estimated by using DFT implemented in VASP by using VASPsol[61,62] as the implicit solvation correction and a three-layer pristine Cu slab. Additional charges were assigned to the unit cell, which congregates on the Cu surface, and a compensating ion charge density in the vacuum space created by VASPsol neutralizes the overall unit cell. The applied potential, U, is computed as below:

$$U \text{ vs. } SHE = -(\mu_e + \varphi)/e$$

where μ_e is chemical potential of electrons, i.e., Fermi level of the system referenced to the vacuum potential, φ is the empirical reference of φ = 4.6 V versus standard hydrogen electrode (SHE) reported in the VASPsol description of the bulk electrolyte.[62] The computed correlation between the surface charge density and the external potential versus SHE is shown in Figure S32 and agrees with the literature.[50]

Electric field and *CO/*OCCO-binding energy

We followed the methodology in the literature[46,47] to derive the correlation between CO-binding energy on Cu(111) slab in vacuum and the external electric field (Figure S30). In addition, we optimized the geometry with CO on Cu(111) with an explicit water layer and a protonated organosuperbase. Once the geometry was relaxed, the electric field, $V_{effective}$, was computed as below:

$$V_{effective} = V_{env} - V_{ion} - V_{solvent} - V_{slab}$$

where V_{env} is the electric field computed with a single-point calculation on the system with a protonated organosuperbase, explicit water molecules, and Cu(111) slab, V_{ion} is the electric field computed with a single-point calculation on the system with a protonated organosuperbase, $V_{solvent}$ is the electric field computed with a single-point calculation on the system with explicit water molecules, V_{slab} is the electric field computed with a single-point calculation on the system with Cu(111) slab. For the calculation of the electric field induced by the deprotonated organosuperbase, we remove the proton binding to the organosuperbase and re-calculate V_{env} and V_{ion}. For the electric field induced by water molecules alone, we re-calculate V_{env} and remove the V_{ion} term in the equation. We obtain $V_{effective}$ at the center of the C–O bond in adsorbed the CO molecule to represent the average electric field that the molecule encounters, whose value was plotted in Figure S30.

To benchmark the CO-binding energy in vacuum, the CO-binding strength with solvent and organosuperbase, $\Delta G_{ads}(CO)$, was computed as below:

$$\Delta G_{ads}(CO) = E_{CO/ion/solvent/slab} - E_{ion/solvent/slab} - G_{CO_{(g)}} + (G_{CO/slab} - E_{CO/slab}) - E_{solvation}$$

Where $E_{CO/ion/solvent/slab}$ is the DFT energy of the optimized geometry with adsorbed CO, protonated/pristine organosuperbase, water molecules, and Cu(111) slab (as shown in Figure 4E), $E_{ion/solvent/slab}$ is a single-point DFT energy after removing the adsorbed CO in the system, $G_{CO}(g)$ is free energy of gaseous CO, $G_{CO/slab} - E_{CO/slab}$ is the free energy correction from the vibrational modes of the adsorbed CO molecule on Cu(111) in vacuum. $E_{solvation}$ is computed as shown below:

$$E_{solvation} = E_{CO/solvent/slab} - E_{solvent/slab} - (E_{CO/slab} - E_{slab})$$

where $E_{CO/solvent/slab}$ is the single-point DFT energy of the system obtained by removing organosuperbase from the optimized geometry, $E_{solvent/slab}$ is the single-point DFT energy of the system obtained by removing organosuperbase and adsorbed CO from the optimized geometry, $E_{CO/slab}$ is the DFT energy of adsorbed CO on Cu(111), $E_{CO/slab}$ is the DFT energy of Cu(111) surface.

SUPPLEMENTAL INFORMATION

Supplemental information can be found online at https://doi.org/10.1016/j.joule.2021.12.002.

ACKNOWLEDGMENTS

This work was supported by Rice University, the ACS PRF # 62074-DNI5, and the Packard Foundation. L.F. acknowledges support from the China Scholarship Council (CSC) (201806320253) and 2018 Zhejiang University Academic Award for Outstanding Doctoral Candidates. T.P.S. and C.-Y.L. acknowledge startup funding from Rice University and support from an InterDisciplinary Excellence Award furnished by the Creative Ventures program at Rice University.

AUTHOR CONTRIBUTIONS

L.F., and C.-Y.L. contributed equally. L.F. and H.W. conceived the project and designed the experiments. H.W. supervised the project. L.F., P.Z., C.X., X.Z., and Z.-Y.W. performed the experimental study. C.-Y.L. and T.P.S. performed the theoretical study. L.F., C.-Y.L., Y.L., T.P.S., and H.W. wrote the manuscript with support from all authors.

DECLARATION OF INTERESTS

The authors declare no competing interests.

Received: September 10, 2021
Revised: December 4, 2021
Accepted: December 7, 2021
Published: December 29, 2021

REFERENCES

1. Seh, Z.W., Kibsgaard, J., Dickens, C.F., Chorkendorff, I., Nørskov, J.K., and Jaramillo, T.F. (2017). Combining theory and experiment in electrocatalysis: insights into materials design. Science *355*, eaad4998.

2. Wu, Y., Jiang, Z., Lu, X., Liang, Y., and Wang, H. (2019). Domino electroreduction of CO2 to methanol on a molecular catalyst. Nature *575*, 639–642.

3. De Luna, P., Hahn, C., Higgins, D., Jaffer, S.A., Jaramillo, T.F., and Sargent, E.H. (2019). What would it take for renewably powered electrosynthesis to displace petrochemical processes? Science *364*, eaav3506.

4. Dunwell, M., Luc, W., Yan, Y., Jiao, F., and Xu, B. (2018). Understanding surface-mediated electrochemical reactions: CO2 reduction and beyond. ACS Catal. *8*, 8121–8129.

5. Verma, S., Lu, S., and Kenis, P.J.A. (2019). Co-electrolysis of CO2 and glycerol as a pathway to carbon chemicals with improved technoeconomics due to low electricity consumption. Nat. Energy *4*, 466–474.

6. Zhang, X., Wang, Y., Gu, M., Wang, M., Zhang, Z., Pan, W., Jiang, Z., Zheng, H., Lucero, M., Wang, H., et al. (2020). Molecular engineering of dispersed nickel phthalocyanines on carbon nanotubes for selective CO2 reduction. Nat. Energy *5*, 684–692.

7. Fan, L., Xia, C., Zhu, P., Lu, Y., and Wang, H. (2020). Electrochemical CO2 reduction to high-concentration pure formic acid solutions in an all-solid-state reactor. Nat. Commun. *11*, 3633.

8. Gu, J., Hsu, C.S., Bai, L., Chen, H.M., and Hu, X. (2019). Atomically dispersed Fe3+ sites catalyze efficient CO2 electroreduction to CO. Science *364*, 1091–1094.

9. Gong, Q., Ding, P., Xu, M., Zhu, X., Wang, M., Deng, J., Ma, Q., Han, N., Zhu, Y., Lu, J., et al. (2019). Structural defects on converted bismuth oxide nanotubes enable highly active electrocatalysis of carbon dioxide reduction. Nat. Commun. *10*, 2807.

10. Möller, T., Scholten, F., Thanh, T.N., Sinev, I., Timoshenko, J., Wang, X., Jovanov, Z., Gliech, M., Roldan Cuenya, B., Varela, A.S., and Strasser, P. (2020). Electrocatalytic CO2 reduction on CuOx nanocubes: tracking the evolution of chemical state, geometric structure, and catalytic selectivity using operando spectroscopy. Angew. Chem. Int. Ed. *59*, 17974–17983.

11. Chen, C., Li, Y., Yu, S., Louisia, S., Jin, J., Li, M., Ross, M.B., and Yang, P. (2020). Cu-Ag tandem catalysts for high-rate CO2 electrolysis toward multicarbons. Joule *4*, 1688–1699.

12. Wang, H., Tzeng, Y.-K., Ji, Y., Li, Y., Li, J., Zheng, X., Yang, A., Liu, Y., Gong, Y., Cai, L., et al. (2020). Synergistic enhancement of electrocatalytic CO2 reduction to C2 oxygenates at nitrogen-doped nanodiamonds/Cu interface. Nat. Nanotechnol. *15*, 131–137.

13. Ting, L.R.L., García-Muelas, R., Martín, A.J., Veenstra, F.L.P., Chen, S.T.-J., Peng, Y., Per, E.Y.X., Pablo-García, S., López, N., Pérez-Ramírez, J., and Yeo, B.S. (2020). Electrochemical reduction of carbon dioxide to

1-butanol on oxide-derived copper. Angew. Chem. Int. Ed. Engl. *59*, 21072–21079.

14. Zhao, K., Nie, X., Wang, H., Chen, S., Quan, X., Yu, H., Choi, W., Zhang, G., Kim, B., and Chen, J.G. (2020). Selective electroreduction of CO2 to acetone by single copper atoms anchored on N-doped porous carbon. Nat. Commun. *11*, 2455.

15. Li, F., Thevenon, A., Rosas-Hernández, A., Wang, Z., Li, Y., Gabardo, C.M., Ozden, A., Dinh, C.T., Li, J., Wang, Y., et al. (2020). Molecular tuning of CO2 -to-ethylene conversion. Nature *577*, 509–513.

16. Montoya, J.H., Shi, C., Chan, K., and Nørskov, J.K. (2015). Theoretical insights into a CO dimerization mechanism in CO 2 electroreduction. J. Phys. Chem. Lett. *6*, 2032–2037.

17. Li, Y., and Sun, Q. (2016). Recent advances in breaking scaling relations for effective electrochemical conversion of CO2. Adv. Energy Mater. *6*, 1600463.

18. Nitopi, S., Bertheussen, E., Scott, S.B., Liu, X., Engstfeld, A.K., Horch, S., Seger, B., Stephens, I.E.L., Chan, K., Hahn, C., et al. (2019). Progress and perspectives of electrochemical CO2 reduction on copper in aqueous electrolyte. Chem. Rev. *119*, 7610–7672.

19. Nam, D.H., De Luna, P., Rosas-Hernández, A., Thevenon, A., Li, F., Agapie, T., Peters, J.C., Shekhah, O., Eddaoudi, M., and Sargent, E.H. (2020). Molecular enhancement of heterogeneous CO2 reduction. Nat. Mater. *19*, 266–276.

20. Ma, M., Djanashvili, K., and Smith, W.A. (2016). Controllable hydrocarbon formation from the electrochemical reduction of CO2 over Cu nanowire arrays. Angew. Chem. Int. Ed. Engl. *55*, 6680–6684.

21. Jiang, K., Sandberg, R.B., Akey, A.J., Liu, X., Bell, D.C., Nørskov, J.K., Chan, K., and Wang, H. (2018). Metal ion cycling of Cu foil for selective C–C coupling in electrochemical CO2 reduction. Nat. Catal. *1*, 111–119.

22. Lee, S.Y., Jung, H., Kim, N.-K., Oh, H.-S., Min, B.K., and Hwang, Y.J. (2018). Mixed copper states in anodized Cu electrocatalyst for stable and selective ethylene production from CO2 reduction. J. Am. Chem. Soc. *140*, 8681–8689.

23. Zhou, Y., Che, F., Liu, M., Zou, C., Liang, Z., De Luna, P., Yuan, H., Li, J., Wang, Z., Xie, H., et al. (2018). Dopant-induced electron localization drives CO2 reduction to C2 hydrocarbons. Nat. Chem. *10*, 974–980.

24. Dinh, C.-T., Burdyny, T., Kibria, M.G., Seifitokaldani, A., Gabardo, C.M., García de Arquer, F.P., Kiani, A., Edwards, J.P., De Luna, P., Bushuyev, O.S., et al. (2018). CO2 electroreduction to ethylene via hydroxide-mediated copper catalysis at an abrupt interface. Science *360*, 783–787.

25. Ma, S., Sadakiyo, M., Luo, R., Heima, M., Yamauchi, M., and Kenis, P.J.A. (2016). One-step electrosynthesis of ethylene and ethanol from CO2 in an alkaline electrolyzer. J. Power Sources *301*, 219–228.

26. Wang, Y., Shen, H., Livi, K.J.T., Raciti, D., Zong, H., Gregg, J., Onadeko, M., Wan, Y., Watson, A., and Wang, C. (2019). Copper nanocubes for CO2 reduction in gas diffusion electrodes. Nano Lett *19*, 8461–8468.

27. García de Arquer, F.P., Dinh, C.-T., Ozden, A., Wicks, J., McCallum, C., Kirmani, A.R., Nam, D.-H., Gabardo, C., Seifitokaldani, A., Wang, X., et al. (2020). CO2 electrolysis to multicarbon products at activities greater than 1 A cm−2. Science *367*, 661–666.

28. Chen, X., Chen, J., Alghoraibi, N.M., Henckel, D.A., Zhang, R., Nwabara, U.O., Madsen, K.E., Kenis, P.J.A., Zimmerman, S.C., and Gewirth, A.A. (2021). Electrochemical CO2-to-ethylene conversion on polyamine-incorporated Cu electrodes. Nat. Catal. *4*, 20–27.

29. Ma, M., Clark, E.L., Therkildsen, K.T., Dalsgaard, S., Chorkendorff, I., and Seger, B. (2020). Insights into the carbon balance for CO2 electroreduction on Cu using gas diffusion electrode reactor designs. Energy Environ. Sci. *13*, 977–985.

30. Verma, S., Hamasaki, Y., Kim, C., Huang, W., Lu, S., Jhong, H.-R.M., Gewirth, A.A., Fujigaya, T., Nakashima, N., and Kenis, P.J.A. (2018). Insights into the low overpotential electroreduction of CO2 to CO on a supported gold catalyst in an alkaline flow electrolyzer. ACS Energy Lett. *3*, 193–198.

31. Jouny, M., Hutchings, G.S., and Jiao, F. (2019). Carbon monoxide electroreduction as an emerging platform for carbon utilization. Nat. Catal. *2*, 1062–1070.

32. Rabinowitz, J.A., and Kanan, M.W. (2020). The future of low-temperature carbon dioxide electrolysis depends on solving one basic problem. Nat. Commun. *11*, 5231.

33. Yan, Z., Hitt, J.L., Zeng, Z., Hickner, M.A., and Mallouk, T.E. (2021). Improving the efficiency of CO2 electrolysis by using a bipolar membrane with a weak-acid cation exchange layer. Nat. Chem. *13*, 33–40.

34. Chen, C., Li, Y., and Yang, P. (2021). Address the "alkalinity problem" in CO2 electrolysis with catalyst design and translation. Joule *5*, 737–742.

35. Ishikawa, T. (2009). Superbases for Organic Synthesis: Guanidines, Amidines and Phosphazenes and Related Organocatalysts (Wiley).

36. van Duin, A.C.T., Dasgupta, S., Lorant, F., and Goddard, W.A. (2001). ReaxFF: a reactive force field for hydrocarbons. J. Phys. Chem. A *105*, 9396–9409.

37. Senftle, T.P., Hong, S., Islam, M.M., Kylasa, S.B., Zheng, Y., Shin, Y.K., Junkermeier, C., Engel-Herbert, R., Janik, M.J., Aktulga, H.M., et al. (2016). The ReaxFF reactive force-field: development, applications and future directions. npj Comput. Mater. *2*, 15011.

38. Aggarwal, V.K., and Mereu, A. (1999). Superior amine catalysts for the Baylis–Hillman reaction: the use of DBU and its implications. Chem. Commun. *1999*, 2311–2312.

39. Grainger, R.S., Leadbeater, N.E., and Masdéu Pàmies, A. (2002). The tetramethylguanidine catalyzed Baylis–Hillman reaction: effects of co-catalysts and alcohol solvents on reaction rate. Catal. Commun. *3*, 449–452.

40. Sorokin, V.I., Ozeryanskii, V.A., and Pozharskii, A.F. (2003). A simple and effective procedure for theN-permethylation of amino-substituted naphthalenes. Eur. J. Org. Chem. *2003*, 496–498.

41. Zhu, P., Xia, C., Liu, C.-Y., Jiang, K., Gao, G., Zhang, X., Xia, Y., Lei, Y., Alshareef, H.N., Senftle, T.P., and Wang, H. (2021). Direct and continuous generation of pure acetic acid solutions via electrocatalytic carbon monoxide reduction. Proc. Natl. Acad. Sci. USA *118*, e2010868118.

42. Becke, A.D. (1988). Density-functional exchange-energy approximation with correct asymptotic behavior. Phys. Rev. A Gen. Phys. *38*, 3098–3100.

43. Lee, C., Yang, W., and Parr, R.G. (1988). Development of the Colle-Salvetti correlation-energy formula into a functional of the electron density. Phys. Rev. B Condens. Matter *37*, 785–789.

44. Marenich, A.V., Cramer, C.J., and Truhlar, D.G. (2009). Universal solvation model based on solute electron density and on a continuum model of the solvent defined by the bulk dielectric constant and atomic surface tensions. J. Phys. Chem. B *113*, 6378–6396.

45. Perdew, J.P., Burke, K., and Ernzerhof, M. (1996). Generalized gradient approximation made simple. Phys. Rev. Lett. *77*, 3865–3868.

46. Chen, L.D., Urushihara, M., Chan, K., and Nørskov, J.K. (2016). Electric field effects in electrochemical CO2 reduction. ACS Catal. *6*, 7133–7139.

47. Resasco, J., Chen, L.D., Clark, E., Tsai, C., Hahn, C., Jaramillo, T.F., Chan, K., and Bell, A.T. (2017). Promoter effects of alkali metal cations on the electrochemical reduction of carbon dioxide. J. Am. Chem. Soc. *139*, 11277–11287.

48. Li, J., Wu, D., Malkani, A.S., Chang, X., Cheng, M.-J., Xu, B., and Lu, Q. (2020). Hydroxide is not a promoter of C2+ product formation in the electrochemical reduction of CO on copper. Angew. Chem. Int. Ed. Engl. *132*, 4494–4499.

49. Wen, J., Ma, T., Zhang, W., van Duin, A.C.T., van Duin, D.M., Hu, Y., and Lu, X. (2019). Atomistic insights into Cu chemical mechanical polishing mechanism in aqueous hydrogen peroxide and glycine: ReaxFF reactive molecular dynamics simulations. J. Phys. Chem. C *123*, 26467–26474.

50. Goodpaster, J.D., Bell, A.T., and Head-Gordon, M. (2016). Identification of possible pathways for C–C bond formation during electrochemical reduction of CO2: new theoretical insights from an improved electrochemical model. J. Phys. Chem. Lett. *7*, 1471–1477.

51. Kresse, G., and Furthmüller, J. (1996). Efficient iterative schemes for *ab initio* total-energy calculations using a plane-wave basis set. Phys. Rev. B Condens. Matter *54*, 11169–11186.

52. Blöchl, P.E. (1994). Projector augmented-wave method. Phys. Rev. B Condens. Matter *50*, 17953–17979.

53. Kresse, G., and Joubert, D. (1999). From ultrasoft pseudopotentials to the projector augmented-wave method. Phys. Rev. B *59*, 1758–1775.

54. Monkhorst, H.J., and Pack, J.D. (1976). Special points for Brillouin-zone integrations. Phys. Rev. B *13*, 5188–5192.

55. Grimme, S., Antony, J., Ehrlich, S., and Krieg, H. (2010). A consistent and accurate *ab initio* parametrization of density functional dispersion correction (DFT-D) for the 94 elements H-Pu. J. Chem. Phys. *132*, 154104.

56. Henkelman, G., Uberuaga, B.P., and Jónsson, H. (2000). A climbing image nudged elastic band method for finding saddle points and minimum energy paths. J. Chem. Phys. *113*, 9901–9904.

57. Rostamikia, G., Mendoza, A.J., Hickner, M.A., and Janik, M.J. (2011). First-principles based microkinetic modeling of borohydride oxidation on a Au(111) electrode. J. Power Sources *196*, 9228–9237.

58. Nie, X., Esopi, M.R., Janik, M.J., and Asthagiri, A. (2013). Selectivity of CO2 reduction on copper electrodes: the role of the kinetics of elementary steps. Angew. Chem. Int. Ed. Engl. *125*, 2519–2522.

59. Akhade, S.A., Bernstein, N.J., Esopi, M.R., Regula, M.J., and Janik, M.J. (2017). A simple method to approximate electrode potential-dependent activation energies using density functional theory. Catal. Today *288*, 63–73.

60. Frisch, M.J., Trucks, G.W., Schlegel, H.B., Scuseria, G.E., Robb, M.A., Cheeseman, J.R., Scalmani, G., Barone, V., Petersson, G.A., Nakatsuji, H., et al. (2016). Gaussian 16. Rev. C.01. https://gaussian.com/relnotes/.

61. Mathew, K., Sundararaman, R., Letchworth-Weaver, K., Arias, T.A., and Hennig, R.G. (2014). Implicit solvation model for density-functional study of nanocrystal surfaces and reaction pathways. J. Chem. Phys. *140*, 084106.

62. Mathew, K., Kolluru, V.S.C., Mula, S., Steinmann, S.N., and Hennig, R.G. (2019). Implicit self-consistent electrolyte model in plane-wave density-functional theory. J. Chem. Phys. *151*, 234101.